Geochemistry, Geophysics, Geosystems

RESEARCH ARTICLE
10.1029/2021GC009663

Key Points:

- Micromagnetic Tomography uniquely recovers higher-order multipole terms for several individual grains in a sample
- Higher order multipole moments are an expression of the internal domain structure of magnetic grains
- Ultimately, this enables to select individual grains for rock- and paleomagnetic studies based on domain configuration

Supporting Information:
Supporting Information may be found in the online version of this article.

Correspondence to:
D. Cortés-Ortuño,
d.i.cortes@uu.nl

Citation:
Cortés-Ortuño, D., Fabian, K., & De Groot, L. V. (2021). Single particle multipole expansions from Micromagnetic Tomography. *Geochemistry, Geophysics, Geosystems*, *22*, e2021GC009663. https://doi.org/10.1029/2021GC009663

Received 19 JAN 2021
Accepted 1 MAR 2021

Single Particle Multipole Expansions From Micromagnetic Tomography

David Cortés-Ortuño[1], Karl Fabian[2], and Lennart V. de Groot[1]

[1]Paleomagnetic Laboratory Fort Hoofddijk, Department of Earth Sciences, Utrecht University, Utrecht, The Netherlands, [2]Norwegian University of Science and Technology (NTNU), Trondheim, Norway

Abstract Micromagnetic tomography aims at reconstructing large numbers of individual magnetizations of magnetic particles from combining high-resolution magnetic scanning techniques with micro X-ray computed tomography (microCT). Previous work demonstrated that dipole moments can be robustly inferred, and mathematical analysis showed that the potential field of each particle is uniquely determined. Here, we describe a mathematical procedure to recover higher orders of the magnetic potential of the individual magnetic particles in terms of their spherical harmonic expansions (SHE). We test this approach on data from scanning superconducting quantum interference device microscopy and microCT of a reference sample. For particles with high signal-to-noise ratio of the magnetic scan we demonstrate that SHE up to order $n = 3$ can be robustly recovered. This additional level of detail restricts the possible internal magnetization structures of the particles and provides valuable rock magnetic information with respect to their stability and reliability as paleomagnetic remanence carriers. Micromagnetic tomography therefore enables a new approach for detailed rock magnetic studies on large ensembles of individual particles.

1. Introduction

Initially, the development of micro- to nanoscale scanning magnetometers for rock- and paleomagnetism aimed at recovering statistical information about the average magnetization of a sample by measuring the surface magnetic signal of the remanence carrying mineral grains (Egli & Heller, 2000; Weiss et al., 2007). One approach is to recover the total dipole moment of a larger sample volume by upward continuation of the magnetic measurements on the surface above this volume to suppress higher-order terms (Fu et al., 2020). Another approach is the spatial domain unidirectional inversion of the magnetization by means of least squares fitting, which relies on constraints to the magnetization vector (Myre et al., 2019; Weiss et al., 2007). A recently developed method of de Groot et al. (2018) improves upon the total moment measurement by aiming to recover the dipole moments of all individual magnetic particles. Although this appears to be unnecessarily complicated, this approach potentially solves almost all problems that haunt paleomagnetism from its early beginnings until today. The most prominent among these problems is mineral alteration, by which the original carriers of the paleomagnetic information change in chemistry or shape and either lose their primary magnetization, or acquire a new magnetization in a different field. Another critical problem is the occurrence of multiple minerals as remanence carriers. If these minerals acquire their magnetization by different processes and with different efficiencies, the mixed natural remanent magnetization may not reflect the paleofield in a straightforward way. The third common problem is a large variation in grain size or domain state of the remanence carrying magnetic mineral by which less reliable multidomain carriers may overprint and invalidate the paleomagnetic signal represented by the more reliable small grain-size fractions of pseudo-single domain or single-domain carriers. By individually determining the magnetic moments of all magnetized grains in a sample, it becomes possible to calculate statistical averages over specifically chosen subsets of optimal remanence carriers. For example, one could remove all particles above a certain grain-size threshold from the statistical ensemble, or disregard all particles with certain unwanted physical or chemical properties, such as all particles below a certain density threshold. The fundamental idea that enables to recover individual particle moments independent from all other moments, is to combine micro X-ray computed tomography (microCT) and scanning magnetometry for rock magnetic measurements. This technique, called Micromagnetic Tomography, has been demonstrated by de Groot et al. (2018). In theory, by adding microCT information, the individual magnetic potentials of topologically separated particles can be recovered from surface measurements of the normal field component on an enclosing sphere, and the corresponding inverse problem even is well-posed in the sense of Hadamard (Fabian & de Groot, 2018). Here, this general result is exploited and experimentally tested by inverting not only for the magnetic dipole moments of the individual particles, but also for higher spherical harmonics, or multipole moments. One advantage of this approach is that it provides additional information about the internal magnetization structure of the particles, even though the well-known nonuniqueness of potential field inversion problems (Zhdanov, 2015) makes it impossible to invert for the magnetization structure itself. For example, multipole inversion may indicate that the particle magnetization is carried by a multi-domain structure rather than by a single-domain structure if the magnetic scanning measurement reveals that the quadrupole and octupole coefficients are much larger than expected for a homogenously magnetized particle. A study by Fu et al. (2020) has recently accounted for the deviation from dipolar behavior (i.e., contribution of higher order moments) in magnetic field maps via the combination of high-resolution Quantum Diamond Microscopy and upward continuation of the field data. Here, multipole moments are fully recovered from the inversions which is facilitated by knowledge of the grain positions. Multipole inversion thus may enable to intrinsically select statistical ensembles of magnetization carriers, based on their internal magnetization structure.

2. Samples and Methods

2.1. Sample and Tomographic Characterization

Tomography and scanning data in this study were acquired from the synthetic sample described in de Groot et al. (2018). It contains natural magnetite particles prepared and described by Hartstra (1982) with diameters between 5 and 35 μm. The particles were embedded in epoxy at approximately 2800 grains per cubic millimeter. Sizes, shapes, and positions of the magnetite grains are recovered from the three-dimensional density distribution within the sample, acquired by microCT (Sakellariou et al., 2004). As described in de Groot et al. (2018), a 1.5 mm × 1.5 mm map of the normal component of the magnetic flux density at a temperature of $T = 4$ K has been measured above the sample using scanning superconducting quantum interference device microscopy (SSM) (Kirtley & Wikswo, 1999). SSM and microCT data are available from the PANGAEA data repository at https://doi.org/10.1594/PANGAEA.886724.

2.2. Inversion Method

The inverse modeling of the magnetic flux density is based on a forward model of the sources, where each particle center is the center of a spherical harmonic expansion (SHE) up to a maximal order n, where $n = 1$ denotes a pure dipole potential, because magnetic potentials contain no monopole contribution. In the test sample, the individual particles are *spherically isolated* in the sense that each particle is contained in a sphere, such that no two of these spheres intersect. This is an essential requirement to ensure that the spherical harmonic potentials are in principle uniquely defined (Fabian & de Groot, 2018). In the following, it is assumed that all sources are spherically isolated. If the individual particles do not fulfill this condition, they have to be grouped, such that the resulting groups are spherically isolated, and the recovered potentials then represent the potentials of these groups.

For the forward calculation, the potentials of all sources are added and the vertical derivative of the combined potential in the scanning $x - y$-plane determines the total vertical field component $B_z(x, y, h)$, where h is the scanning height of the sensor loop. The flux through the sensor is obtained by integrating this field component over the sensor area in the $x - y$-plane. By this procedure, the sensor signal in the forward model is represented by a linear combination of the SHE coefficients of all particles. If the number of measurements is larger than the number of these expansion coefficients, the design matrix M of the system becomes over-determined for the expansion coefficients, and a least-square fit of these coefficients can be obtained via the pseudoinverse of M.

A single magnetic particle inside a volume V corresponds to a distribution of volume charges $\lambda\left(\mathbf{r}\right)$ ($\lambda = 0$ outside V), where $\mathbf{r}$ is the position vector within the source. Its magnetic scalar potential at a location $\mathbf{R}$ outside the smallest sphere that contains V reads

$$\Phi(\mathbf{R}) = \gamma_B \int_V \frac{\lambda(\mathbf{r})}{\left|\mathbf{R}-\mathbf{r}\right|} \mathrm{d}^3 r, \tag{1}$$

where $\gamma_B = \mu_0 (4\pi)^{-1}$. When the observation point $\mathbf{R}$ is far away from the magnetic source, that is, $R \gg r$, with R and r the magnitudes of the position vectors, the expansion of $\left|\mathbf{R}-\mathbf{r}\right|^{-1}$ in terms of R^{-1} leads to the Cartesian multipole expansion of Φ as

$$\begin{aligned}\gamma_B^{-1}\Phi(\mathbf{R}) = {} & \underbrace{(-1)\left[\int_V \mathrm{d}^3 r \lambda(\mathbf{r}) r_i\right] \frac{\partial}{\partial R_i}\frac{1}{R}}_{\text{dipole}} \\ & + \underbrace{\frac{(-1)^2}{2!}\left[\int_V \mathrm{d}^3 r \lambda(\mathbf{r}) r_i r_j\right] \frac{\partial^2}{\partial R_i \partial R_j}\frac{1}{R}}_{\text{quadrupole}} \\ & + \underbrace{\frac{(-1)^3}{3!}\left[\int_V \mathrm{d}^3 r \lambda(\mathbf{r}) r_i r_j r_k\right] \frac{\partial^3}{\partial R_i \partial R_j \partial R_k}\frac{1}{R}}_{\text{octupole}} + \mathcal{O}\left(r^4\right)\end{aligned} \tag{2}$$

where R_i and r_i for $i = 1, 2, 3$ are the Cartesian components of $\mathbf{R}$ and $\mathbf{r}$, respectively, and repeated indexes follow Einstein's summation convention. Again, the expansion starts with the dipole term because there are no magnetic monopoles. In Cartesian coordinates, all nth-order derivatives of R^{-1} have the form

$$p(R_1, R_2, R_3) R^{-n-1}, \tag{3}$$

where p is a homogeneous nth-order harmonic polynomial. The vector space spanned by these polynomials has a basis of $2n + 1$ linearly independent elements as a subspace of the space of all nth-order homogeneous polynomials. By defining a scalar product of two polynomials p, q as the average over the unit sphere by

$$\langle p, q\rangle = \frac{1}{4\pi}\int_{r=1} p(\mathbf{r})\, q(\mathbf{r})\, dS, \tag{4}$$

it turns out that the nth-order derivative polynomials are not orthogonal. To correct this problem, both the terms with derivatives and the terms with integrals are expressed as tensors. The derivative tensor is traceless for $n > 1$ because $1/R$ is harmonic outside the sphere. The integral tensor defines the corresponding multipole coefficients of the charge distribution.

The product of these two tensors can be transformed to the basis of real spherical harmonics, which transforms the polynomials into a completely orthogonal set of basis functions. The resulting multipole expansions can be written as

$$\gamma_B^{-1}\Phi(\mathbf{R}) = \sum_{n=1}^{3}\sum_{\alpha=1}^{2n+1} \Theta_\alpha^{t(n)} Q^{\alpha(n)}(\mathbf{R}) + \mathcal{O}\left(r^4\right), \tag{5}$$

where $\Theta_\alpha^{t(n)}$ are the components of the traceless magnetic multipole tensor of rank n and $Q^{\alpha(n)}(\boldsymbol{R})$ are the spherical harmonic polynomials that decay as $R^{-(n+1)}$. The here applied mathematical formalism (Applequist, 2002; Burnham & English, 2019; Stone, 2013) is detailed in Appendix and Section S8 of the supporting information. The corresponding nth-order multipole terms of the magnetic field $\mathbf{B}(\mathbf{R}) = -\nabla\Phi(\mathbf{R})$ decay proportional to $R^{-(n+2)}$. The first (dipole), second (quadrupole), and third (octupole) order contributions $B_k^{(n)}$, for $n = 1, 2, 3$ are listed in Appendix.

For any maximal multipole order n, an approximation of the field can be constructed, where the field created by each particle at each measurement point is represented by its $n\,(n+2)$ independent multipole coefficients. Based on these coefficients, a $L \times \left(n(n+2)K\right)$ forward matrix is constructed that models the magnetic flux from the K magnetic sources to multipole order n at each of the L measurement points i as

$$B^{(\text{scan})}_{z|i} = \sum_{j=1}^{K} B^{(\text{particle})}_{z|i,j} = \gamma_B \sum_{j=1}^{K} \left[P^{\alpha(1)}_{z|i,j} \cdot \Theta^{t(1)}_{\alpha|j} + P^{\alpha(2)}_{z|i,j} \cdot \Theta^{t(2)}_{\alpha|j} + P^{\alpha(3)}_{z|i,j} \cdot \Theta^{t(3)}_{\alpha|j} \right], \tag{6}$$

with $P^{\alpha(n)}_{z|i,j} = -\partial Q^{\alpha(n)}_{i,j} \,/\, \partial z$ as the derivative of the spherical harmonic polynomials for particle j at measurement point i and $\Theta^{t(n)}_{\alpha|j}$ the rank-n multipole tensor components of particle j. The polynomials for the z-component of the magnetic field B_k are again orthogonal. Because only B_z is used in the inversion, this orthogonality implies that the SHE bases of each particle are uncorrelated, which should lead to numerically favorable properties.

The best-fit multipole coefficients of the sources are then computed via the pseudoinverse of this rectangular design matrix, which corresponds to the linear least-square fit of the measurement data, as long as $L > n\,(n+2)\,K$.

3. Results

3.1. Tomography and Magnetic Scanning

To analyze the effectiveness of the multipole expansion technique, solutions for the SSM measurements reported in de Groot et al. (2018) are obtained by solving the inversion problem in the three areas depicted in Figures 1b–1d. To validate the calculations applied to real samples, test problems for the inversion of dipole signals as a function of grain position, grain depth, and field scan noise, have been developed and are described in Section S1 of the supporting information.

In de Groot et al. (2018), magnetic grains are modeled as aggregations of cubes with a constant magnetization and locations specified by microCT image analysis. This allowed to uniquely solve for homogeneous magnetizations in each of these spherically separated grains. Unique source assignment of the potential-field signal in this kind of system is a well-posed inverse problem (Fabian & de Groot, 2018). The uniqueness is not restricted to the dipole moments, but extends to the potential field of each grain, and thus to all SHE coefficients. The essential constraint of the uniqueness theorem is that the complement of the source regions must be simply connected (Fabian & de Groot, 2018). This excludes the possibility to reconstruct signals from source regions inside other source regions, and makes it unfeasible to obtain detailed complex magnetization structures like multidomain structures. Yet, the multipole expansion of the potential may suffice to distinguish between a finite number of physically possible local energy minimum structures that can be modeled based on grain shape and mineralogy. The coefficients of the multipole expansion can be found for particles for which the smallest enclosing sphere is completely below the scan surface to ensure the validity of the far-field potential description (3) at the measurement points. These coefficients describe point sources representing the magnetic particles. A natural choice for the origins of the multipole expansions are the geometric centers of the particles outlined by their microCT density anomaly with respect to the surrounding matrix. Alternatively, the expansion center may be chosen as the center of the smallest sphere that contains the particle, but the choice of the expansion center does not influence the reconstructed *dipole* coefficients.

The three-dimensional image in Figure 1a visualizes the relation between the scanning surface and the position of the magnetite grains for Area 1. The plots below, Figures 1b–1d, depict the original measurement data for three areas from the SSM scan together with the particle boundaries as determined by microCT. The magnetic states in the magnetic sources correspond to the initial state after preparation of the sample, CT measurement and cooling in the SQUID magnetometer, and are considered as random magnetization states without prior information in the inversion process. The row of images in Figures 1e–1g shows the modeled B_z signals for the inversions of Area 1 to stepwise increasing multipole-expansion orders from $n = 1$ (dipole, left) to $n = 3$ (octupole, right). The bottom row, Figures 1h–1j, depicts the maps of the corresponding residuals.

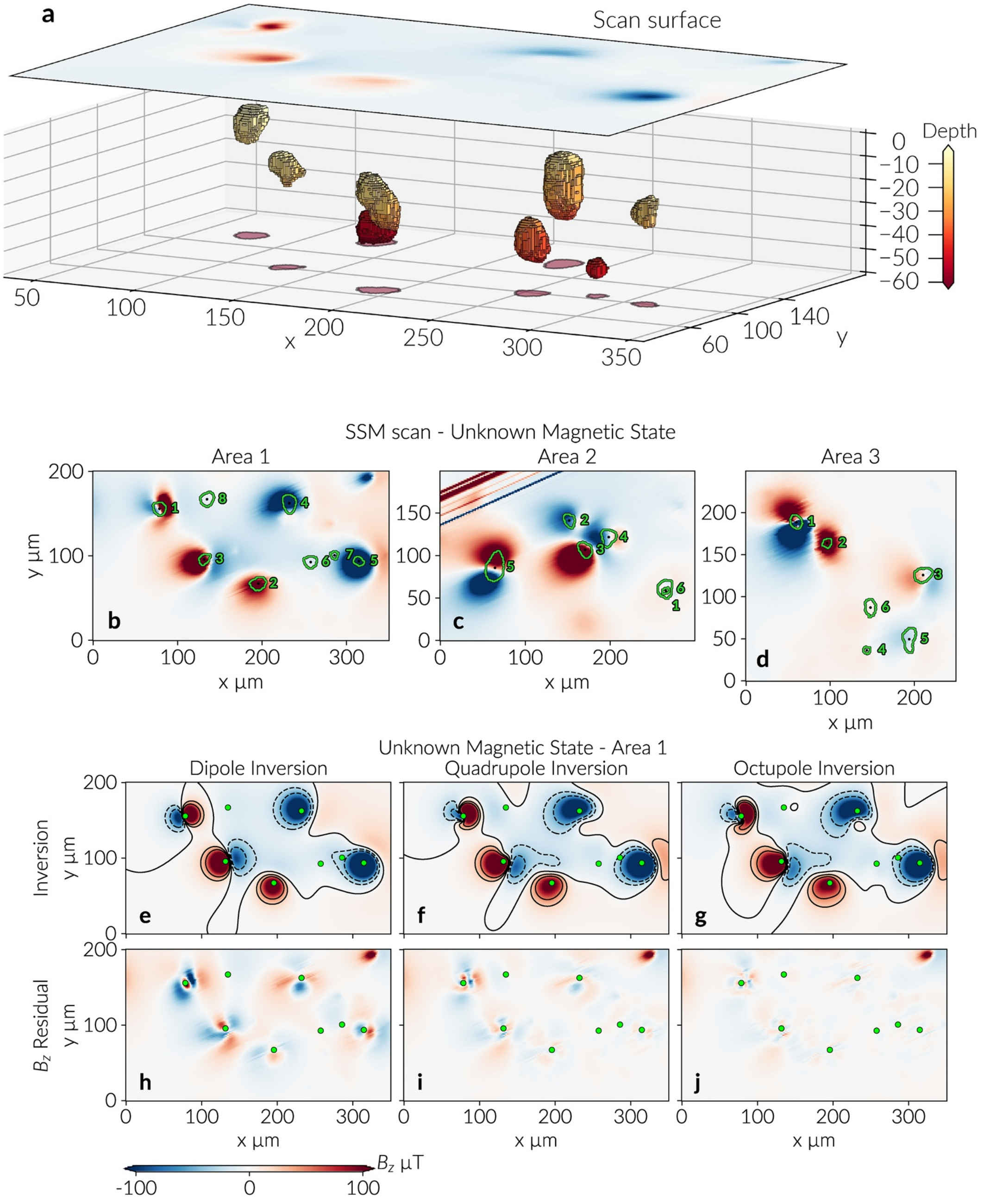

Figure 1. Multipole inversion from Micromagnetic Tomography. (a) Three-dimensional view of the surface-scan region in relation to the voxel images of the magnetite grains beneath Area 1. (b–d) Two-dimensional surface SSM scan data for the initial magnetic states from de Groot et al. (2018) over sample areas 1–3 with projected particle boundaries (green) from nanotomography. (e–g) Stepwise inverted B_z fields for Area 1 of the SSM scan using multipole expansions up to dipole (left), quadrupole (center), and octupole (right) order. Contour lines range from -50 µT up to 50 µT in steps of 25 µT. (h–j) Residuals after removing the inverted B_z fields for Area 1 from the measured data. Particle centers are indicated by green circles.

A first test for the consistency of the inversions is to compare the dipole moments recovered by inversions at different multipole orders. From the inverted dipole moments for the particles in areas 1–3 the resulting average volume magnetizations are computed and summarized in Figures 2d–2f, using the saturation magnetization of magnetite as reference. The magnetization values obtained by multipole inversion are compared to the results of de Groot et al. (2018) for the same particles. The magnetization values obtained

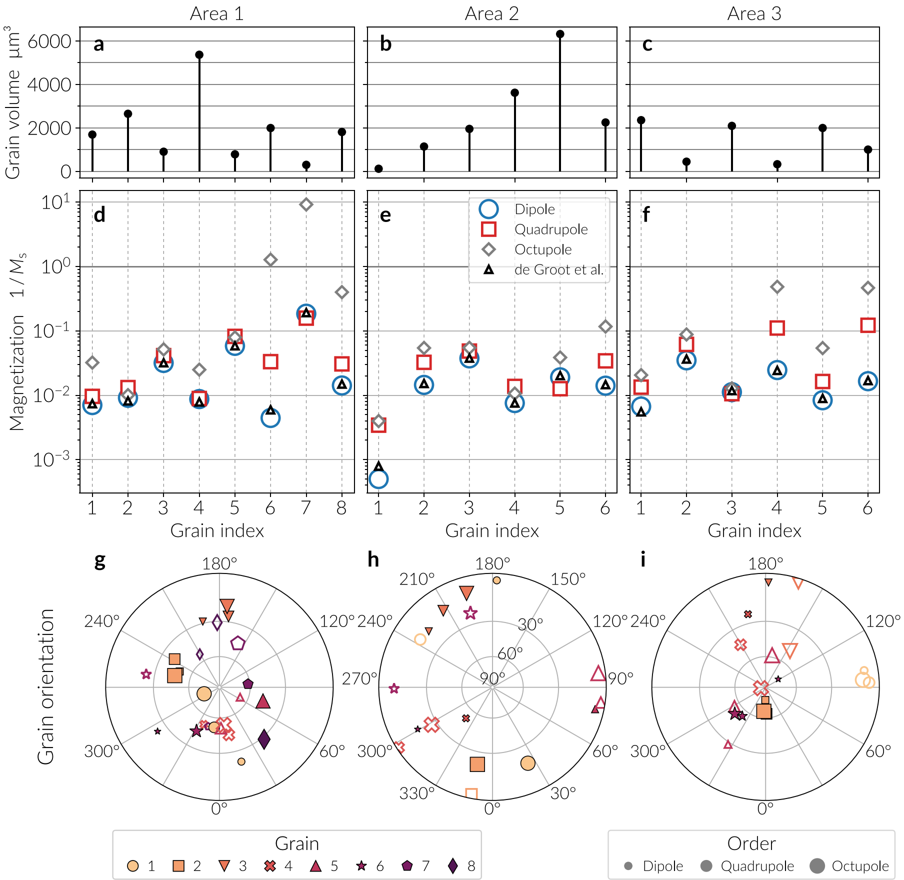

Figure 2. Grain magnetizations, orientations, and volumes. Comparison of multipole inversions at different orders by means of magnetization calculations are shown in (d–f). Magnetization values are normalized by the saturation magnetization of magnetite M_s and are compared to those of de Groot et al. (2018). Orientations of the grain magnetizations are depicted in (g–f) using an stereographic projection. Polar angles are measured from the equator and with negative value angles in the southern hemisphere shown as open markers. Orientations from increasing multipole order inversions are distinguished with markers of increasing size. Grain volumes are reported in the top subplots (a–c).

from the lowest-order (dipole) inversion agree very well with the homogeneous magnetization inversions of de Groot et al. (2018). In Area 1, for instance, the relative errors range from 0.17% (grain 5) to 12% (grain 2), with the exception of grain 6 which has a large error of 25%. In de Groot et al. (2018), each particle is represented by up to 442 cuboids to estimate its homogeneous magnetization vector. The far-field representation of grains as point-dipole sources requires substantially fewer numerical calculations and is computationally much more effective in simulating the scan signal.

Table 1
Inversion Results for Two Grains of Area 1

	Grain 1			Grain 5		
Order	Max(res) µT	Max (B_z^{inv}) µT	RMSE	Max(res) µT	Max (B_z^{inv}) µT	RMSE
Dipole	−180.08	308.48	41.53	74.97	−379.75	19.41
Quadrupole	−100.01	383.35	19.61	−30.77	−377.70	5.61
Octupole	−72.65	410.40	10.84	−37.85	−372.24	4.12

Note. Residual, inversion and root mean square error (RMSE) of grains 1 and 5 within a 30 µm radius around the grain centers. Inversions are performed using multipole expansions at different orders.

The residuals near the strongly expressed grains 1–5 in Area 1 of Figure 1h are large compared to the dipole signal. Table 1 lists that, for example, within a radius of 30 µm around grain 5 the largest residual value is approximately 26% of the largest signal magnitude (see Sections S5–S7 in the supporting information for the other grains and areas). These high residuals demonstrate that the dipole approximation only explains a part of the measured signal, and that higher order harmonics are required to optimally describe the potential of the magnetic source distribution inside the particles. Inversion results in Figures 1f and 1g belong to models with expansion up to quadrupole and octupole moments, respectively. Their residuals are shown in Figures 1i and 1j. With the higher-order s

moments the largest signal of grain 5 keeps its magnitude but the residual of the quadrupole expansion decreases to less than half the value for the dipole expansion, and remains similar for the octupole expansion (see Table 1). The improvement due to the octupole expansion is more evident in grain 1. For the quadrupole expansion, the largest residual for this grain decreases to 56% of the maximum value of the dipolar signal, and to 40% for the octupole expansion. Similar tendencies are observed for grains 2–4. Although the residual does not significantly decrease with higher order terms, it is roughly an order of magnitude smaller than the B_z signal from the expansion up to the octupole order. Around grains 1 and 3, the residual after removing the octupole expansion is still noticeable, with magnitudes of 72.65 and 65.72 μT, respectively. This indicates that more complex multidomain structures are better visible in these particles because they lie closest to the scan surface (see Figure 3). Apparently, proximity to the measurement surface and signal strength are critical for resolving higher order multipole moments of the grains. This will be confirmed by analyzing the signal of grains 6 to 8.

The average volume magnetizations from the quadrupole expansion in Figure 2d agree well with those inferred from the dipole expansion. For grains 1–3 and 5 the relative errors are in average 38% while grain 4 has the smallest variation with 2% (see Table S1). When octupole terms are included, deviations become significant for grains 6 and 7, and possibly grain 8. These grains generate the weakest signals in Figure 1g and pose the greatest challenge for the numerical inversion. This is observed, in particular, from the relatively high magnitudes of the normalized magnetization in Figure 2d. The residuals in Figures 1i and 1j for grains 6–8 are of similar size and substantially smaller than for striped residuals at other locations. This indicates that the inherent noise level inhibits an improved recovery of their higher multipole coefficients and that correlated noise leads to artificially overestimated magnetization.

In addition to the magnetization magnitudes, the spherical angles defining the vector components of the magnetization (or dipolar moments) are recovered from the multipole inversions and are depicted in Figures 2g–2i for the three analyzed areas and for increasing multipole expansion orders (numerical values are shown in Section S4 in the supporting information). In the case of Area 1, shown in Figure 2g, the orientations of grains 2–4 vary slightly with the different multipole orders. For instance, the dipole-inversion magnetization of grain 2 (square markers) is oriented with the polar and azimuthal angles (49.06°, 248.24°). By increasing the multipole expansion order, the quadrupole-inversion and octupole-inversion magnetization vectors deviate by 11.41° and 5.62°, respectively, with respect to the dipole order vector (i.e., $\arccos(\mathbf{m} \cdot \mathbf{m}_{\text{dipole}})$ with $\mathbf{m} = \mathbf{M}/|\mathbf{M}|$). In contrast, the octupole-inversion magnetizations for grain 1 and 5 have larger deviations of 67.4° and 114.14°, respectively. Moreover, the polarity of the magnetization of grain 5 is reversed with an octupole order inversion. This result supports the idea of grains 2–4 having simple domain structures with a dominant dipolar component, and substantiates the hypothesis of more complex magnetic orderings existing in grains 1 and 5. In the case of grains 6–8, deviations are significant and confirm the bad behavior of the numerical inversion with a weak field signal.

A first estimation of the quality of the inverted grain magnetizations, previous to a numerical inversion, can be deduced from the expected dipole signal. For a grain with volume V at a depth d from the scan surface this signal is proportional to the scaling factor (see Appendix for details)

$$b_{\text{dip}} = \mu_0 M_{\text{s}} \frac{V}{d^3}. \tag{7}$$

with M_{s} as the saturation magnetization of magnetite. Intuitively, grains deep in the sample will have a small b_{dip} which can be compensated by the grain size. The scaling factor is depicted in Figure 3a as a function of grain depth, confirming that grains with the weakest signal, and thus with multipole inversions with large deviations, are the farthest in distance from the surface. Grain 1, on the contrary, has the strongest factor owing to its proximity to the surface, although Figure 2 shows it suffers from deviations of the dipole moment with an octupole expansion. Similarly, grain 5 exhibits a strong scan signal; however, its b_{dip} magnitude is the smallest among the shallower grains.

Analyzing the signal-to-noise ratio (SNR) of the dipole signal, which is the strongest moment contribution, provides an extra criteria to characterize the reliability of the multipole inversion on every grain. The SNRs are shown in Figure 3a for Area 1 of the SSM data. To calculate the SNR of a grain, a point dipole source

Table 2
Cartesian Components of the Quadrupole Field Polynomials

$p_x^{1(2)} = -\sqrt{\frac{3}{2}}x\left(R^2 - 5z^2\right)$	$p_y^{1(2)} = -\sqrt{\frac{3}{2}}y\left(R^2 - 5z^2\right)$	$p_z^{1(2)} = \sqrt{\frac{3}{2}}z\left(5z^2 - 3R^2\right)$
$p_x^{2(2)} = -\sqrt{2}z\left(R^2 - 5x^2\right)$	$p_y^{2(2)} = 5\sqrt{2}xyz$	$p_z^{2(2)} = -\sqrt{2}x\left(R^2 - 5z^2\right)$
$p_x^{3(2)} = 5\sqrt{2}xyz$	$p_y^{3(2)} = -\sqrt{2}z\left(R^2 - 5y^2\right)$	$p_z^{3(2)} = -\sqrt{2}y\left(R^2 - 5z^2\right)$
$p_x^{4(2)} = \frac{1}{\sqrt{2}}x\left(3R^2 - 5\left(2y^2 + z^2\right)\right)$	$p_y^{4(2)} = \frac{1}{\sqrt{2}}y\left(7R^2 - 5\left(2y^2 + z^2\right)\right)$	$p_z^{4(2)} = \frac{5}{\sqrt{2}}z(x - y)(x + y)$
$p_x^{5(2)} = -\sqrt{2}y\left(R^2 - 5x^2\right)$	$p_y^{5(2)} = -\sqrt{2}x\left(R^2 - 5y^2\right)$	$p_z^{5(2)} = 5\sqrt{2}xyz$

is generated from the dipole moments of a dipole inversion (up to third order R^{-3} in the expansion of the field). Then, a rectangular area around the source is defined by surrounding the field contours containing 90% of the dipole signal. This area is used as the signal matrix B_z^{dip} and is shown in Figures 3b and 3d for grains 2 and 6, respectively. The noise matrix in this context is given by the residual of the inversion that has all dipole signals removed, and because the expansion comprises only dipolar terms the residual contains the contributions of higher-order moments in addition to the measurement uncertainties from the noise of the scan signal, which partly is spatially uncorrelated but also may be partly correlated. The ratio between the Frobenius norm $\| \cdot \|_F$ of these signal and noise matrices gives an estimation of the dipole field B_z^{dip} energy contribution of a grain. In Figure 3a, the SNRs are plotted as a function of grain depth and it is clear that below a critical depth the SNRs decrease radically. In particular, grains 6 and 8 have SNRs smaller than

Table 3
Cartesian Components of the Octupole Field Polynomials

$p_x^{1(3)} = \sqrt{\frac{5}{2}}xz\left(7z^2 - 3R^2\right)$	$p_y^{1(3)} = \sqrt{\frac{5}{2}}yz\left(7z^2 - 3R^2\right)$	$p_z^{1(3)} = \frac{1}{\sqrt{10}}\left(3R^4 + 35z^4 - 30R^2z^2\right)$
$p_x^{2(3)} = -\frac{1}{2}\sqrt{\frac{3}{5}}\left(4R^4 - 5R^2\left(y^2 + 7z^2\right) + 35z^2\left(y^2 + z^2\right)\right)$	$p_y^{2(3)} = -\frac{1}{2}\sqrt{15}xy\left(R^2 - 7z^2\right)$	$p_z^{2(3)} = \frac{1}{2}\sqrt{15}xz\left(7z^2 - 3R^2\right)$
$p_x^{3(3)} = -\frac{1}{2}\sqrt{15}xy\left(R^2 - 7z^2\right)$	$p_y^{3(3)} = \frac{1}{2}\sqrt{\frac{3}{5}}\left(R^4 - 5R^2\left(y^2 + z^2\right) + 35y^2z^2\right)$	$p_z^{3(3)} = \frac{1}{2}\sqrt{15}yz\left(7z^2 - 3R^2\right)$
$p_x^{4(3)} = \sqrt{\frac{3}{2}}xz\left(5R^2 - 7\left(2y^2 + z^2\right)\right)$	$p_y^{4(3)} = \sqrt{\frac{3}{2}}yz\left(9R^2 - 7\left(2y^2 + z^2\right)\right)$	$p_z^{4(3)} = -\sqrt{\frac{3}{2}}\left(R^2 - 7z^2\right)(x^2 - y^2)$
$p_x^{5(3)} = -\sqrt{6}yz\left(R^2 - 7x^2\right)$	$p_y^{5(3)} = -\sqrt{6}xz\left(R^2 - 7y^2\right)$	$p_z^{5(3)} = -\sqrt{6}xy\left(R^2 - 7z^2\right)$
$p_x^{6(3)} = \frac{1}{2}\left(-3x^2\left(7y^2 + z^2\right) + 4x^4 + 3y^2\left(y^2 + z^2\right)\right)$	$p_y^{6(3)} = \frac{1}{2}xy\left(13R^2 - 7\left(4y^2 + z^2\right)\right)$	$p_z^{6(3)} = \frac{7}{2}xz\left(x^2 - 3y^2\right)$
$p_x^{7(3)} = -\frac{1}{2}xy\left(28y^2 + 21z^2 - 15R^2\right)$	$p_y^{7(3)} = \frac{1}{2}\left(3R^2\left(9y^2 + z^2\right) - 3R^4 - 7\left(3y^2z^2 + 4y^4\right)\right)$	$p_z^{7(3)} = -\frac{7}{2}yz\left(y^2 - 3x^2\right)$

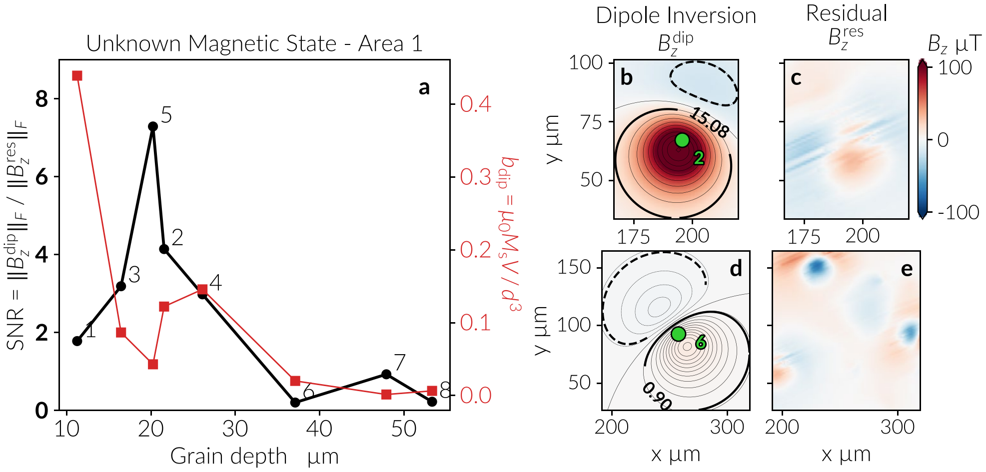

Figure 3. Signal-to-noise ratio (SNR) and dipole field scaling factor as a function of grain depth. The SNR magnitudes are shown in (a) with circle markers and are computed using inversions up to the dipole order in a square area around grains that covers 90% of the dipole signal. Both the dipole signal and residual (noise) from the inversion are shown in (b) and (c), respectively, for grain 2, and in (d) and (e) for grain 6. Contours enclosing 90% of the positive and negative dipole signal are shown in (b) and (d). The dipole factors b_{dip} are depicted in (a) with square markers and refer to the right vertical axis. Numbers at the SNR data points indicate grain indices.

one. This is in agreement with the tendency of the scaling factor b_{dip}. Results of SNR calculations for Area 2 and 3 (see Section S4 in supporting information) also show that below a depth of approximately 30 µm the SNRs decrease significantly. Although grain 1 of Area 1 has a strong signal, as depicted in Figure 1e, its SNR is smaller than those of grains 2–5, which could be due to its proximity to the scan surface. This suggests that the far-field approximation is probably not optimal and either an inner-field description or higher order harmonics are needed for a better description. This poorly resolved inversion also explains the difference from the large b_{dip} factor that indicated a high SNR could be associated to grain 1. An additional parameter that might be affecting the inversion result is the grain size, which is shown in Figures 2a–2c for the three SSM scan areas. It is observed that grain 7 of Area 1 has the smallest volume with a low SNR, and similarly for grain 1 of Area 2 (see supporting information). Furthermore, by comparison to grain 1, grain 5 has the largest SNR with a low b_{dip}, suggesting that grain size can have a significant impact on the numerical inversion. Nevertheless, to statistically determine the importance of volume size in both the scan signal and thus the quality of the inversion, more experimental data is necessary.

4. Discussion

4.1. Inversion for the Spherical Harmonic Expansion

The results show that solving for higher multipole expansions of the potential of individual magnetic grains reduces the residual from the numerical inversions that recover the magnetic signal of individual grains. Considering higher multipole orders beyond the dipole approximation improves the reconstruction of the measured signal and refines the magnitude of the recovered grain magnetizations. The achievable improvement significantly depends on the signal-quality of the scanning measurement. The experimental data agree with the theoretical prediction that grains exhibiting a weak signal (cf. grains 6–8 in Area 1, Figure 1b) are either smaller or located deeper in the sample, beyond the magnetometer sensitivity, which is in contrast to comparable grains with stronger signals (cf. grains 1, 3, 5 in Area 1, Figure 1b). The multipole inversion in the here studied application becomes ineffective below a threshold depth of approximately at 30 µm beneath the sample surface. If grains are located below each other, the signals of the deeper grains can be shadowed even if the grains are spherically separated. This does not reflect an intrinsic nonuniqueness, but rather the fact that such constellations lead to an ill-conditioned design matrix with high noise-amplification for the deep grains. In contrast, shallow grains are generally well resolved and their inverted multipole moments are numerically stable. A direct solution to strengthen the signal of deep grains experimentally,

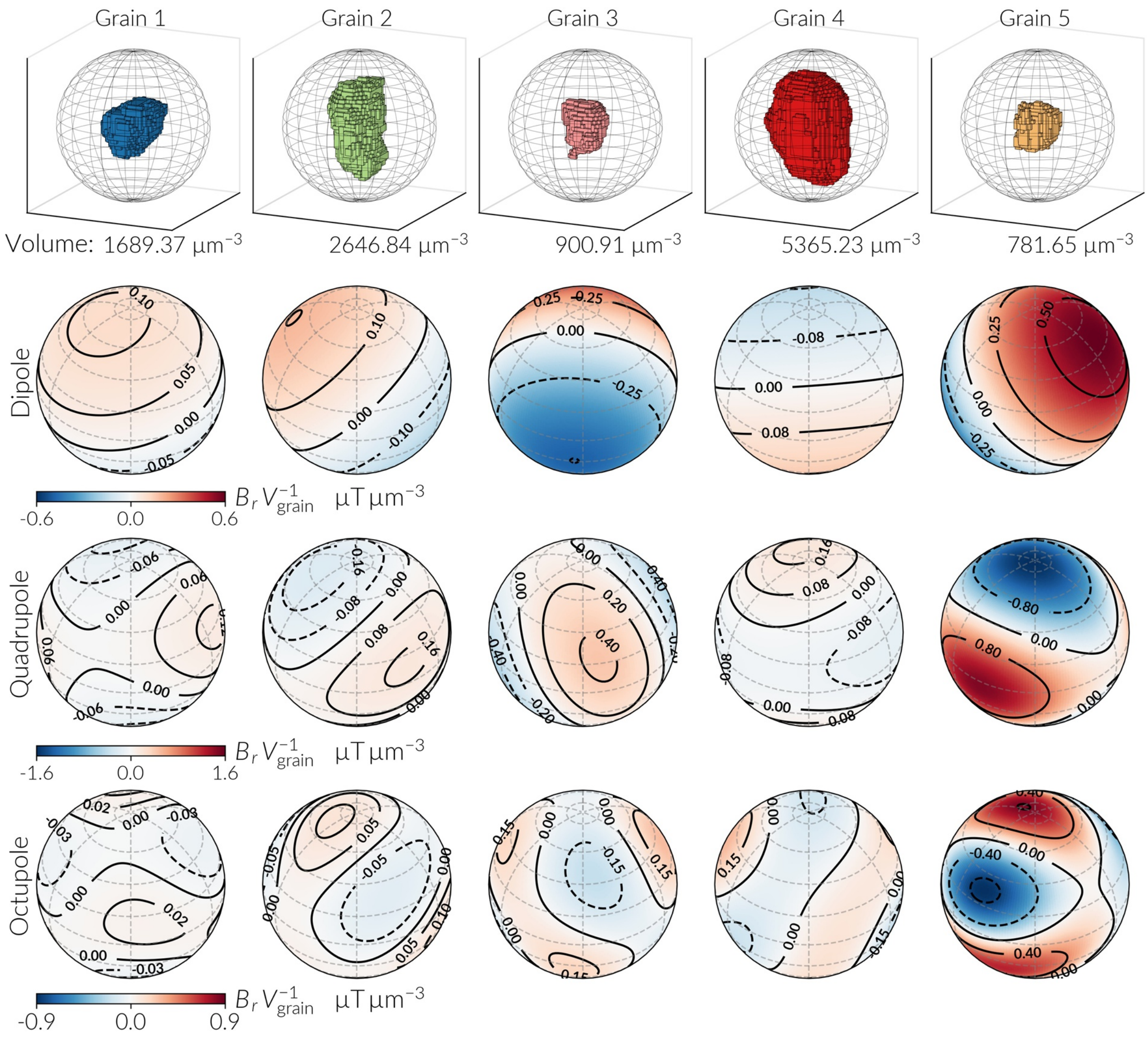

Figure 4. Grain profile and radial multipole fields of particles 1–5 in Area 1. The top row shows the geometry of the grains with bounding spheres of 20 μm, radius. Spheres are defined at the geometric center of each particle, around which the potential of the particle is represented by a SHE. The three rows below depict the radial field of each particle, reconstructed from the SSM data. The fields are orthographically projected at the surface of the bounding spheres for the first three multipole expansion terms, which are specified to the left. Field magnitudes are scaled by the particle volumes, shown below the grain profiles.

and thus improve the numerical inversions, is to scan the sample from opposite sides. This might also allow to verify the well-behaved inversions.

The inversion results were analyzed by displaying the radial field on a bounding sphere around selected individual magnetite grains. Reliable results are obtained for grains with a strong signal that are numerically stable at inversions of increasing multipole orders. The radial field at the sphere surface uniquely determines the potential field at any point outside the sphere. Thus, all coefficients of the exterior SHE of the potential are determined by the radial field component, which thereby contains all outside available information about the sources within the sphere (Blakely, 1996). Figure 4 individually depicts the corresponding radial fields for the multipole moments of order $n = 1$, 2, and 3 computed from an octupole inversion for grains 1–5 in Area 1.

For all grains, the same radius of 20 μm was chosen for the bounding sphere. To account for the volume differences of the grains, field magnitudes are scaled by the grain volume, specified at the top row of Figure 4, and thus given in units of Tm^{-3}. This volume scaling explains why the smallest grain 5 can have the strongest field signal at all three multipole orders, with a dominant quadrupole signal. Its strong field variation at higher orders also suggests that grain 5 possesses a relatively complex magnetization structure. A similar complexity at higher orders is observed in grain 3 although with a weaker volume-normalized field. Grain 4 also exhibits a distinct octupole character, but this is less perceptible due to its large volume, which probably allows for highly efficient flux-closure by a multidomain magnetization structure. Also grain 1 is clearly in the multidomain grain size region, although its higher-order fields appear less dominant than in the other grains. Its quadrupole field is of similar order of magnitude as its dipole field, and it was observed that this grain showed a remarkable reduction of the inversion residual for $n > 1$.

5. Conclusions

Here, we describe a new method for rock and paleomagnetism to reconstruct higher multipole moments of individual particles from surface scans of the magnetic field in combination with microCT. The method is based on a previous mathematical proof that the corresponding linear inverse problem is well-posed. We here provide numerical and experimental evidence that the reconstruction is technically possible, and define a set of conditions that need to be met to robustly infer dipole, quadrupole, and octupole moments for individual particles. We also provide analytical parameters to compare dipole and higher-order moments, that allow to infer marginal domain-state information. This might be validated in future studies by means of computational micromagnetic modeling, as has been previously used to confirm complex orderings in magnetic grains from experimental imaging (Shah et al., 2018). In this context, our study enables future rock magnetic and paleomagnetic studies to characterize and select natural mineral grains based on their domain configuration.

Appendix

Magnetic Field from Multipole Expansion

The k-component of the magnetic field of an individual grain, at a point sufficiently far away from the magnetic source, can be written as an expansion in terms of a minimal set of real and orthogonal spherical harmonics. This has been proved in (Burnham & English, 2019) by generalizing the results of Applequist (2002), who defined the so-called Maxwell-Cartesian spherical harmonic polynomials that appear in the expansion of the potential using Cartesian coordinates. Additionally, Burnham and English specify the orthogonal spherical harmonic basis by adapting the polynomials from Stone (2013). According to this, the field can be written as

$$B_k = \sum_{n=1}^{\infty} B_k^{(n)} = \gamma_B \sum_{n=1}^{\infty} \sum_{\alpha=1}^{2n+1} \Theta_{\alpha}^{t(n)} P_k^{\alpha(n)}$$

The $2n + 1$ multipole polynomials $P_k^{\alpha(n)} = -\partial Q^{\alpha(n)} / \partial R_k$, which are in the basis of spherical harmonics, can be computed by deriving the real harmonics of Burnham and English (2019) using Mathematica or the open source SymPy library. By defining

$$p_k^{\alpha(n)} = R^{2n+3} P_k^{\alpha(n)},$$

The three Cartesian components of the quadrupole field polynomials ($n = 2$) are summarized in Table 2 and the octupole field polynomials ($n = 3$) are shown in Table 3. According to this, it is customary to obtain the radial field components as $B_r = B_x \sin\theta \cos\varphi + B_y \sin\theta \sin\varphi + B_z \cos\theta$, where the spherical angles are computed with respect to every grain center (the multipole point source).

Signal Scale

Consider the ith particle with volume V_i and saturation magnetization M_s at depth d_i. Dependent of its magnetization structure, its average magnetization is $|\mathbf{M}_i| = \alpha_i M_s$ with a geometric factor $\alpha_i \leq 1$. Its magnetic dipole moment is therefore $\mu_i = \alpha_i M_s V_i$ and at distance d_i it generates a component B_z that scales according to

$$\mu_0 \frac{\mu_i}{r_i^3} = \alpha \, \mu_0 \, M_{\mathrm{s}} \frac{V_i}{d_i^3}.$$

Accordingly, the B_z contribution of the 2-nd order SHE coefficient scale proportional to

$$b_{\mathrm{dip}}(d_i, V_i) = \mu_0 \, M_{\mathrm{s}} \frac{V_i}{d_i^3}.$$

Data Availability Statement

The data used in this study are the same data as used in de Groot et al. (2018), and are available from the PANGAEA data repository at https://doi.org/10.1594/PANGAEA.886724. Numerical calculations were performed using the Numpy (Harris et al., 2020), SciPy (Virtanen et al., 2020), Matplotlib (Hunter, 2007), Shapely (Gillies et al, 2007), and Cartopy (Met Office, 2010 - 2015, 2015) Python libraries, and symbolic calculations were obtained with Wolfram Mathematica (Wolfram Research, Inc., 2020).

Acknowledgments
This project has received funding from the European Research Council (ERC) under the European Union's Horizon 2020 research and innovation program (Grant agreement No. 851460 to L. V. d. Groot).

References

Applequist, J. (2002). Maxwell–Cartesian spherical harmonics in multipole potentials and atomic orbitals. *Theoretical Chemistry Accounts*, *107*(2), 103–115. https://doi.org/10.1007/s00214-001-0301-2

Blakely, R. J. (1996). *Potential theory in gravity and magnetic applications*. Cambridge University Press. Retrieved from https://www.cambridge.org/nl/academic/subjects/earth-and-environmental-science/solid-earth-geophysics/potential-theory-gravity-and-magnetic-applications?format=PB

Burnham, C. J., & English, N. J. (2019). A new relatively simple approach to multipole interactions in either spherical harmonics or cartesians, suitable for implementation into Ewald Sums. *International Journal of Molecular Sciences*, *21*(1), 277. https://doi.org/10.3390/ijms21010277

de Groot, L. V., Fabian, K., Béguin, A., Reith, P., Barnhoorn, A., & Hilgenkamp, H. (2018). Determining individual particle magnetizations in assemblages of micrograins. *Geophysical Research Letters*, *45*(7), 2995–3000. https://doi.org/10.1002/2017GL076634

Egli, R., & Heller, F. (2000). High-resolution imaging using a high-T-c superconducting quantum interference device (SQUID) magnetometer. *Journal of Geophysical Research-Solid Earth*, *105*, 25709–25727.

Fabian, K., & de Groot, L. V. (2018). A uniqueness theorem for tomography-assisted potential-field inversion. *Geophysical Journal International*, *216*(2), 760–766. https://doi.org/10.1093/gji/ggy455

Fu, R. R., Lima, E. A., Volk, M. W. R., & Trubko, R. (2020). High-sensitivity moment magnetometry with the quantum diamond microscope. *Geochemistry, Geophysics, Geosystems*, *21*(8), e2020GC009147. https://doi.org/10.1029/2020GC009147

Gillies, S., Bierbaum, A., Lautaportti, K., & Tonnhofer, O., (2007). *Shapely: Manipulation and analysis of geometric objects*. Retrieved from https://github.com/Toblerity/Shapely

Harris, C. R., Millman, K. J., van der Walt, S. J., Gommers, R., Virtanen, P., Cournapeau, D., et al. (2020). Array programming with NumPy. *Nature*, *585*(7825), 357–362. https://doi.org/10.1038/s41586-020-2649-2

Hartstra, R. (1982). Grain-size dependence of initial susceptibility and saturation magnetization-related parameters of four natural magnetites in the PSD-MD range. *Geophysical Journal of the Royal Astronomical Society*, *71*, 477–495.

Hunter, J. D. (2007). Matplotlib: A 2D graphics environment. *Computing in Science & Engineering*, *9*(3), 90–95. https://doi.org/10.1109/MCSE.2007.55

Kirtley, J. R., & Wikswo, J. P. (1999). Scanning squid microscopy. *Annual Review of Materials Science*, *29*(1), 117–148. https://doi.org/10.1146/annurev.matsci.29.1.117

Met Office. (2010 - 2015). *Cartopy: A cartographic python library with a Matplotlib interface*. Exeter, Devon. Retrieved from https://scitools.org.uk/cartopy/docs/latest/citation.html

Myre, J. M., Lascu, I., Lima, E. A., Feinberg, J. M., Saar, M. O., & Weiss, B. P. (2019). FEB 4). Using TNT-NN to unlock the fast full spatial inversion of large magnetic microscopy data sets. *Earth Planets and Space*, *71*. https://doi.org/10.1186/s40623-019-0988-8}

Sakellariou, A., Sawkins, T. J., Senden, T. J., & Limaye, A. (2004). X-ray tomography for mesoscale physics applications. *Mechanics and its Applications*, *339*(1–2), 152–158. https://doi.org/10.1016/j.physa.2004.03.055

Shah, J., Williams, W., Almeida, T. P., Nagy, L., Muxworthy, A. R., Kovács, A., et al. (2018). The oldest magnetic record in our solar system identified using nanometric imaging and numerical modeling. *Nature Communications*, *9*(1), 1173. https://doi.org/10.1038/s41467-018-03613-1

Stone, A. (2013). *The theory of intermolecular forces* (2nd ed.). Oxford University Press. https://doi.org/10.1093/acprof:oso/9780199672394.001.0001

Virtanen, P., Gommers, R., Oliphant, T. E., Haberland, M., Reddy, T., Cournapeau, D., & SciPy 1.0 Contributors. (2020). SciPy 1.0: Fundamental algorithms for scientific computing in Python. *Nature Methods*, *17*, 261–272. https://doi.org/10.1038/s41592-019-0686-2

Weiss, B. P., Lima, E. A., Fong, L. E., & Baudenbacher, F. J. (2007). Paleomagnetic analysis using squid microscopy. *Journal of Geophysical Research*, *112*, B09105. https://doi.org/10.1029/2007JB004940

Wolfram Research, Inc. (2020). *Mathematica, Version 12.1*. Champaign, IL. Retrieved from https://www.wolfram.com/mathematica

Zhdanov, M. S. (2015). *Inverse theory and applications in geophysics* (2nd ed.). Elsevier.